Space: Science & Technology
A SCIENCE PARTNER JOURNAL

RESEARCH ARTICLE

Deployment of Three-Body Chain-Type Tethered Satellites in Low-Eccentricity Orbits Using Only Tether

Cheng Jia[1,2], Zhongjie Meng[1,2*], and Bingheng Wang[3]

[1]School of Astronautics, Northwestern Polytechnical University, Xi'an 710072, China. [2]National Key Laboratory of Aerospace Flight Dynamics, Northwestern Polytechnical University, Xi'an 710072, China. [3]Department of Electrical and Computer Engineering, National University of Singapore, Singapore 117583, Singapore.

*Address correspondence to: mengzhongjie@nwpu.edu.cn

Citation: Jia C, Meng Z, Wang B. Deployment of Three-Body Chain-Type Tethered Satellites in Low-Eccentricity Orbits Using Only Tether. *Space Sci. Technol.* 2023;3:Article 0070. https://doi.org/10.34133/space.0070

Submitted 30 June 2023
Accepted 21 August 2023
Published 18 September 2023

Copyright © 2023 Cheng Jia et al. Exclusive licensee Beijing Institute of Technology Press. No claim to original U.S. Government Works. Distributed under a Creative Commons Attribution License 4.0 (CC BY 4.0).

The tethered TSAR (tomographic synthetic aperture radar) system is a group of tethered SAR satellites that can be rapidly deployed and provide a stable baseline for 3-dimensional topographic mapping and moving target detection. Successful deployment is critical for TSAR tethered system. This paper discusses the deployment strategy for a 3-body chain-type tethered satellite system in a low-eccentric elliptical orbit. Two deployment strategies are discussed. Then, the tension on the tether is used to deploy it to the desired length and suppress its sway motion, resulting in an underactuated and input-constrained system. Hierarchical sliding mode control (HSMC) with anti-windup technology is employed to overcome the above challenges. In addition, the proposed approach includes the use of a disturbance observer to estimate the second derivative signal and a robust differentiator to estimate the sliding surfaces of the unacted subsystem. Finally, the effectiveness of the proposed deployment strategy is verified by MATLAB/Simulink.

Introduction

Recently, an abundance of the latest technology, such as synthetic aperture radar (SAR), has been introduced into Earth remote sensing. The TanDEM-X space radar interferometer, launched in 2010 and consisting of 2 TerraSAR-X radars flying in close formation, can obtain a globally consistent digital elevation model (DEM) with unparalleled accuracy [1,2]. During the mission, the second satellite needs to adjust its relative configuration through orbital maneuvers to meet coverage requirements and form a stable and effective baseline. In contrast, the tethered interferometric SAR (InSAR) [3] proposed in the 1990s provides a relatively stable, long, and variable baseline throughout the orbital cycle and at all latitudes. Moreover, it does not require heavy orbital maneuvers and therefore consumes less fuel. In addition, the tethered satellite system (TSS) takes only a few hours to build up the interferometric configuration. Besides, the multi-tethered chain-type satellite system could provide a multi-baseline for tomographic SAR (TSAR) to form a real 3-dimensional imaging. Since these potential merits of TSS, it has been used in Earth observations [4], space interferometry [2] and other space missions [5–7].

A well-executed deployment of TSS is a prerequisite for space missions. Numerous control techniques have been proposed in the literature over the years. These techniques can be classified into several categories according to their control mode, including length control [8], length rate control [9], tension control, and thrust-aided control [10,11]. The length control or length rate control method is usually simple enough to give its analytical expression, and is convenient to implement by the reel mechanism. However, these strategies are likely to fail because tether tension is unknown in the deployment process, which can lead to the following 2 undesirable phenomena: (a) The tether may break under excessive tension, and (b) tether may be slack and bounce when tension is negative. Adjusting tension is a more reasonable and promising option than using thrusters due to the latter's high energy consumption and installation complexity. However, the strong nonlinearity and underactuated characteristics of tether pose additional challenges for tension control. What is more, as is mentioned before, maintaining tension within a positive range during deployment is crucial to prevent breakage or slackness. Ma et al. [12] proposed an adaptive sliding mode controller to tackle the underactuated control problem while incorporating tension constraint for TSS deployment. Xu et al. [13] developed a fuzzy controller based on rigorous mathematical foundations, in which the asymmetric constraint on tether tension was addressed. By decoupling the underactuated system into 2 subsystems, Xu et al. [14] designed a fractional-order sliding surface for the actuated subsystem and an integer order for the unactuated subsystem. Considering the nonnegative deployment velocity constraint, Murugathasan and Zhu [15] transformed the velocity constraint into an invariant property of tether deployment dynamics and developed a tension controller. Although there are various tether deployment schemes, most literature focuses on 2-body TSS, with little emphasis on multi-TSSs.

Downloaded from https://spj.science.org at North China Electric Power University on July 31, 2024

Previous studies of multi-TSSs have focused on triangular [16,17], hub-spoke formation [18], and space elevator [19]. In the above studies, space tethers have been applied to various space missions, such as orbital transfer and satellite deorbit. Compared to these missions, the tethered TSAR system has unique requirements for system configuration. First, tomographic imaging requires multiple baselines to obtain high resolution in the height dimension, and 3 or more satellites are needed. Second, the tether should be distributed along the local vertical for DEM to maintain a stable baseline by the gravity gradient and along the local horizontal for GMTI (ground moving target indication). Third, TSAR's baseline, which is determined by tether length and distribution, requires only a few hundred meters or even shorter. What is more, the TSS for SAR always runs in an elliptical orbit; hence, it is necessary to pay attention to the complete motion control of TSS (including orbital motion). Unfortunately, converging the full state to zero by adjusting the tension only, as stated in [19], is challenging due to the underactuated feature. Therefore, the complete motion control of TSS using only the tether has not been discussed in the above literature. Finally, the TSAR baseline needs to be dynamically adjusted to meet different measurements [20] by slightly changing the tether length through the reel mechanism [21] and removing the negative deployment velocity constraint in our work.

This paper proposes a deployment scheme for a 3-body chain-type TSS in elliptical orbit using only tethers, as it is a typical multi-TSS. First, 2 separation approaches for TSS (sequential or simultaneous) are tested and the controllability of the system is verified. Then, a 3-layer sliding surface is delivered for the underactuated model of TSS. In addition, an anti-windup module has been added to address the tension constraint. Due to sensor noise and unmeasurable acceleration signals, a disturbance observer (DO) was implemented to estimate the second derivative of tether length and libration angle. The sliding manifold of the non-actuated orbital motion subsystem was estimated using a robust differentiator. Finally, the effectiveness of the proposed algorithm is verified by numerical simulation.

The paper is structured as follows: The "Modeling of 3-Body TSS" section establishes the motion model of a 3-body chain-type TSS in a low-eccentric elliptical orbit. In the "Deployment Strategies and Controllability Analysis" section, the effects of deployment strategy and controllability using only tension for TSS are investigated. The "Tether Deployment Controller Design" section introduces a novel hierarchical sliding mode control (HSMC) deployment law. The "Numerical Simulation" section covers simulation setup and results. Finally, conclusions are drawn in the "Conclusions" section.

Notations: The stenography sig is defined as $\mathrm{sig}^b(a) = |a|^b \cdot \mathrm{sign}(a)$, the mark $\mathrm{sign}_{relay}(\sigma, \varepsilon)$ indicates the sigmoid function $\sigma \cdot (|\sigma| + \varepsilon)^{-1}$, and sign(·) stands for the signum function.

Modeling of 3-Body TSS

In this section, we will establish the motion model for the 3-body TSS (3 satellites connected by 2 independent tethers). To simplify the problem and highlight the major dynamic features, 2 assumptions are made.

(a) The tethers are massless as their weight is negligible compared to that of the end bodies due to their short length (only a few hundred meters).

(b) Only the planar motion is considered, since the out-of-plane is almost zeros when no thrust is acted in the TSS system [22] Moreover, the coupling of in-plane and out-of-plane motion is not obvious during the deployment process.

The proposed model consists of 3 point masses (m_1, m_2, and m_3) and 2 massless tethers (L_1 and L_2), as illustrated in Fig. 1. The orbit of m_1 is defined by its orbital geocentric distance r and true anomaly α, while the position of m_2 relative to m_1 is determined by tether L_1 and in-plane libration angle θ_1. Additionally, the position of m_3 relative to m_2 is determined by L_2 and θ_2.

The dynamic model of 3-body TSS is derived using Lagrangian formulation [23], and the motion equations in the Euler–Lagrange form are expressed as

$$\mathbf{M}(\mathbf{q})\ddot{\mathbf{q}} + \mathbf{C}(\mathbf{q}, \dot{\mathbf{q}})\dot{\mathbf{q}} + \mathbf{G}(\mathbf{q}) = \mathbf{Q} \tag{1}$$

where generalized coordinates $\mathbf{q} = (r, \alpha, \theta_1, \theta_2, L_1, L_2)^T$, $\mathbf{G}$ is the gravitational forces vectors, Coriolis and centrifugal force matrix is denoted by $\mathbf{C}$, and $\mathbf{M}$ corresponds to the inertial matrix and is given by

$$\mathbf{M} = \begin{pmatrix} m_1+m_2+m_3 & M_{12} & M_{13} & M_{14} & M_{15} & m_3\cos\theta_2 \\ M_{21} & M_{22} & M_{23} & M_{24} & M_{25} & M_{26} \\ M_{31} & M_{32} & (m_2+m_3)L_1^2 & M_{34} & 0 & M_{36} \\ M_{41} & M_{42} & M_{43} & m_3L_2^2 & M_{45} & 0 \\ M_{51} & M_{52} & 0 & M_{54} & m_2+m_3 & M_{56} \\ m_3\cos\theta_2 & M_{62} & M_{63} & 0 & M_{65} & m_3 \end{pmatrix}$$

$\mathbf{C}$, $\mathbf{G}$ and elements of $\mathbf{M}$ are given in supplemental materials.

Environmental perturbation forces in low Earth orbit, such as atmospheric drag and solar radiation pressure, are negligible compared to tether tensions. Therefore, the nonconservative force $\mathbf{Q}$ in Eq. 1 can be generalized

$$\begin{cases} Q_r = Q_\alpha = Q_{\theta_1} = Q_{\theta_2} = 0 \\ Q_{L_1} = -T_1 \\ Q_{L_2} = -T_2 \end{cases} \tag{2}$$

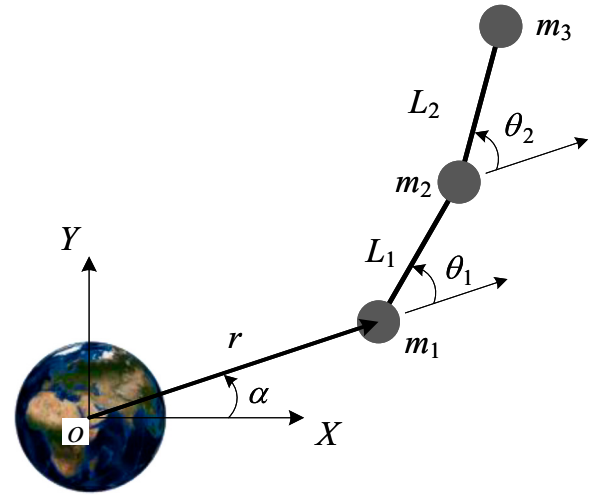

Fig. 1. Model of 3-body chain-type tethered satellite system.

Downloaded from https://spj.science.org at North China Electric Power University on July 31, 2024

where $\mathbf{Q} = (Q_r, Q_a, Q_{\theta_1}, Q_{\theta_2}, Q_{L_1}, Q_{L_2})^T$ and T_1 and T_2 are tether tensions for the system.

Obviously, the TSS model in Eq. 1 is a typical underactuated systems for it has 6 DOFs (degrees of freedom) but only 2 inputs. For the underactuated TSS system in Eq. 1, the generalized coordinates can be decomposed as

$$\mathbf{q} = \left(\mathbf{q}_a, \mathbf{q}_{ua}\right)^T \tag{3}$$

where $\mathbf{q}_a = (L_1, L_2)^T$ is the actuated configuration vectors and $\mathbf{q}_{ua} = (r, \alpha, \theta_1, \theta_2)^T$ is the unactuated configuration vectors.

Deployment Strategies and Controllability Analysis

Tether Deployment Strategies

Rewrite the equation of θ_1 as follows:

$$\begin{aligned}
&\left(m_2+m_3\right)\left[L_1\left(\ddot{\alpha}+\ddot{\theta}_1\right)+2\dot{L}_1\left(\dot{\alpha}+\dot{\theta}_1\right)+\right.\\
&\left.(r\ddot{\alpha}+2\dot{r}\dot{\alpha})\cos\theta_1-\left(\ddot{r}-r\dot{\alpha}^2\right)\sin\theta_1\right]+\\
&m_3\left\{\left[L_2\left(\ddot{\alpha}+\ddot{\theta}_2\right)+2\dot{L}_2\left(\dot{\alpha}+\dot{\theta}_2\right)\right]\cos\left(\theta_1-\theta_2\right)-\right.\\
&\left.\left[\ddot{L}_2-L_2\left(\dot{\alpha}+\dot{\theta}_2\right)^2\right]\sin\left(\theta_1-\theta_2\right)\right\}-\\
&\mu\left\{\frac{m_2 r\sin\theta_1}{R_2^3}+\frac{m_3\left[r\sin\theta_1+L_2\sin\left(\theta_1-\theta_2\right)\right]}{R_3^3}\right\}=Q_{\theta_1}
\end{aligned} \tag{4}$$

By analyzing Eq. 4, it can be concluded that the tether deployment rate $\dot{L}_1, \dot{L}_2$, geocentric distance r, orbital angular velocity $\dot{\alpha}$, and libration velocity $\dot{\theta}_2$, and their derivatives, will affect angular motion θ_1. In the above factors, $\dot{L}_1, \dot{L}_2, \dot{\theta}_2$ is related to the tether deployment scheme, and $\dot{r}, \dot{\alpha}$ is determined by orbital eccentricity. Wang et al. [24] states that the satellite's libration motion is limited to a circular path and tends to converge toward the local vertical with a reduction in eccentricity. In addition, the chain-type TSS needs to be separated several times to complete the deployment, and each separation will affect the deployed tether due to the coupling between adjacent tethers. Therefore, the deployment method with different separation strategies should be carefully chosen.

To deploy the TSS along the local vertical direction, there are 2 separation approaches: (a) All satellites are separated at the same time and (b) satellites are ejected one by one. For the first approach, small initial deviations would cause collisions between satellites, which is undesirable for TSS missions. For the second method, the new satellite will be separated only after the completion of the previous deployment, which can effectively avoid the collision risk due to the small distance in the early stages. In addition, by dividing the TSS system into several 2-body elements, the deployment techniques used for a 2-body system can be applied directly to the single element. Therefore, the latter separation approach is adopted in this paper.

After determining the separation strategy, a subsequent question is to design a deployment law to (a) deploy the tether to a given distance and (b) reduce the oscillation amplitude of the tether. There are 2 main categories for deployment strategies: (a) planning an optimal off-line deployment trajectory, which cannot handle uncertain initial conditions and external disturbances, and optimization complexity increases with the number of satellites and (b) designing a close-loop controller to counteract the adverse impact of (a). In practice, optimization results obtained by (a) are generally used as reference commands of (b). Here, a simple and efficient deployment scheme, combining exponential and uniform deployment law, is selected.

$$\dot{L}_{ci}(t) = \begin{cases} c_i L_{si} & \left(L_{0i} \le L_{ci} \le L_{si}\right) \\ c_i\left(L_{si} - L_{ci}(t)\right) & \left(L_{si} < L_{ci} \le L_{fi}\right) \end{cases} \tag{5}$$

where c_i is a constant, L_{0i} and L_{fi} represent the initial and final lengths, respectively, and L_{si} is the switch length, $i = 1, 2$. Compared with the scheme proposed in [25], the exponential acceleration period is removed because the tether is only a hundred-length tether for SAR.

Integring Eq. 5 yields $\boldsymbol{q}_{ca} = (L_{c1}, L_{c2})^T$, and defining the desired unactuated vectors as $\boldsymbol{q}_{cua} = (r_c, \alpha_c, \theta_{c1}, \theta_{c2})^T$, combined with Eq. 1, one can obtain

$$\boldsymbol{M}\left(\boldsymbol{q}_c\right)\ddot{\mathbf{q}}_c + \boldsymbol{C}\left(\boldsymbol{q}_c, \dot{\mathbf{q}}_c\right)\dot{\mathbf{q}}_c + \boldsymbol{G}\left(\boldsymbol{q}_c\right) = 0 \tag{6}$$

where $\theta_1 = \theta_2 \equiv 0$ to make the tether along the gravity gradient direction.

Then, the normal commands can be obtained by integring Eq. 6, and the control objective is to achieve trajectory tracking using tether tension.

Controllability analysis

The state controllability is studied in this subsection. Poincaré's recurrence theorem, Poisson stability, and the Lie algebra rank condition (LARC) are used to analyze the controllability of underactuated TSS system.

Let, $\mathbf{x}_1 = \mathbf{q}, \mathbf{x}_2 = \dot{\mathbf{q}}$ the motion model of TSS (Eq. 1) can be converted to the following state space form

$$\dot{\mathbf{x}} \triangleq \begin{pmatrix} \dot{\mathbf{x}}_1 \\ \dot{\mathbf{x}}_2 \end{pmatrix} = \mathbf{f}(\mathbf{x}) + \mathbf{g}(\mathbf{x})\mathbf{u} \tag{7}$$

where

$$\mathbf{f}(\mathbf{x}) = \begin{pmatrix} \mathbf{x}_2 \\ -\mathbf{M}(\mathbf{x}_1)_{-1}\left(\mathbf{C}(\mathbf{x}_1, \mathbf{x}_2)\mathbf{x}_2 + \mathbf{G}(\mathbf{x}_1)\right) \end{pmatrix}, \mathbf{g}(\mathbf{x}) = \begin{pmatrix} \mathbf{0}_{6\times 1} \\ \mathbf{M}\left(\mathbf{x}_1\right)^{-1}\mathbf{b} \end{pmatrix},$$
$$\mathbf{u} = \left(T_1, T_2\right)^T$$

According to the results in [26,27], the process for controllability analysis can be divided into 2 steps. First, $\mathbf{f}(\mathbf{x})$ should be weakly positively Poisson stable (WPPS); then, if LARC is satisfied, the underactuated TSS system is controllable.

If no constraint-preserving force acts on the underactuated TSS system described in Eq. 7, the flow generated by $\mathbf{f}(\mathbf{x})$ is volume-preserving. Also, the system's energy remains bounded, preventing its state from evolving to infinity within a finite time. This implies that $\mathbf{f}(\mathbf{x})$ satisfies the WPPS condition based on Poincaré's recurrence theorem.The next step is to demonstrate that the system meets LARC, and the following Lie brackets are considered.

$$\begin{aligned}
&\left\{\mathbf{g}_1, \mathbf{g}_2,\right.\\
&\left[\mathbf{f}, \mathbf{g}_1\right], \left[\mathbf{f}, \mathbf{g}_2\right],\\
&\left[\mathbf{g}_1, \left[\mathbf{f}, \mathbf{g}_1\right]\right], \left[\mathbf{g}_2, \left[\mathbf{f}, \mathbf{g}_2\right]\right],\\
&\left[\mathbf{f}, \left[\mathbf{g}_1, \left[\mathbf{f}, \mathbf{g}_1\right]\right]\right], \left[\mathbf{f}, \left[\mathbf{g}_2, \left[\mathbf{f}, \mathbf{g}_2\right]\right]\right],\\
&\left[\mathbf{g}_1, \left[\mathbf{f}, \left[\mathbf{g}_1, \left[\mathbf{f}, \mathbf{g}_1\right]\right]\right]\right], \left[\mathbf{g}_2, \left[\mathbf{f}, \left[\mathbf{g}_2, \left[\mathbf{f}, \mathbf{g}_2\right]\right]\right]\right],\\
&\left.\left[\mathbf{f}, \left[\mathbf{g}_1, \left[\mathbf{f}, \left[\mathbf{g}_1, \left[\mathbf{f}, \mathbf{g}_1\right]\right]\right]\right]\right], \mathbf{f}, \left[\mathbf{g}_2, \left[\mathbf{f}, \left[\mathbf{g}_2, \left[\mathbf{f}, \mathbf{g}_2\right]\right]\right]\right]\right\}
\end{aligned} \tag{8}$$

Downloaded from https://spj.science.org at North China Electric Power University on July 31, 2024

where $[\mathbf{f},\mathbf{g}]=\frac{\partial \mathbf{g}}{\partial \mathbf{x}}\mathbf{f}-\frac{\partial \mathbf{f}}{\partial \mathbf{x}}\mathbf{g}$ is the definition of Lie bracket. The complete results in Eq. 8 are uniquely defined, are complicated but easily calculated with a computer, and are omitted here for conciseness. It is evident that the matrix is full rank, which indicates that the LARC is satisfied. Therefore, the underactuated TSS is controllable.

Tether Deployment Controller Design

As discussed in the "Deployment Strategies and Controllability Analysis" section, coupling between adjacent tethers should be considered in deployment control. During the deployment process, positive tension must be guaranteed due to the characteristic tether, and to avoid tether rupture, tension could not exceed the given boundaries. To address this limitation, a controller was designed for accurate trajectory tracking. As suggested in the "Deployment Strategies and Controllability Analysis" section, the control objective is to allow libration errors to approach zero when the tether is fully deployed and to minimize orbital tracking error.

Due to inherent robustness, no model transformation is required, and the particular hierarchical structure is particularly suitable for the underactuated system. HSMC is adopted in our work. In addition, there are still 3 problems to be solved.

(a) Tension saturation, mitigated by an auxiliary system;

(b) The unavailable second derivative signal $\ddot{\mathbf{q}}$, estimated by a DO;

(c) The uncertainty of sliding surface and its time derivative for orbit motion (r,α), estimated by a sliding mode-based robust differentiator.

The controller framework is shown in Fig. 2.

First, for the actuated vector $\mathbf{q}_a$, the following auxiliary system is introduced to mitigate the input saturation caused by tether tension constraint

$$\begin{cases}\dot{\lambda}_1=-k_1\lambda_1+\lambda_2\\ \dot{\lambda}_2=-k_2\lambda_2+g_1\Delta u_1\\ \dot{\lambda}_3=-k_3\lambda_3+\lambda_4\\ \dot{\lambda}_4=-k_4\lambda_4+g_2\Delta u_2\end{cases}\tag{9}$$

where $k_i>0$, λ_i is the state variable of the auxiliary system, for $i=1, 2, \cdots, 4$, $\Delta u_i=\mathrm{sat}(u_i)-u_i$ for $i=1, 2$, and $\mathrm{sat}(\cdot)$ is the saturation function.

To construct the error variables of actuated subsystems with the auxiliary system, the following variables are given by

$$\begin{cases}e_1=e_{L_1}-\lambda_1\\ e_2=\dot{e}_{L_1}+k_1\lambda_1-\lambda_2\\ e_3=e_{L_2}-\lambda_3\\ e_4=\dot{e}_{L_2}+k_3\lambda_3-\lambda_3\end{cases}\tag{10}$$

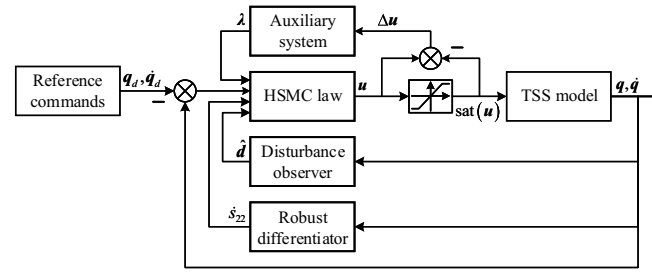

Fig. 2. Schematic of the deployment control framework.

where $e_{L_1}=L_1-L_{1d}$, $e_{L_2}=L_2-L_{2d}$.

By differentiating Eq. 10 with respect to time and substituting Eqs. 1 and 9, the following expression is obtained:

$$\begin{cases}\dot{e}_1=e_2\\ \dot{e}_2=g_1\left(u_1-f_{L_1}-d_{L_1}\right)-\ddot{L}_{1d}-k_1^2\lambda_1+\left(k_1+k_2\right)\lambda_2\\ \dot{e}_3=e_4\\ \dot{e}_4=g_2\left(u_2-f_{L_2}-d_{L_2}\right)-\ddot{L}_{2d}-k_3^2\lambda_3+\left(k_3+k_4\right)\lambda_4\end{cases}\tag{11}$$

where $g_1^{-1}=M_{55}=m_2+m_3$, $g_2^{-1}=M_{66}=m_3$. The terms $d_{L_1}=\sum_{j=1}^{6}M_{5j}\ddot{q}_j-M_{55}\ddot{L}_1$, $d_{L_2}=\sum_{j=1}^{6}M_{6j}\ddot{q}_j-M_{66}\ddot{L}_2$ regroup the second derivative parts in Eq. 1, which is not available and is difficult to construct from the system states. f_{Li} are the remaining parts of the dynamics in Eq. 1, for $i=1, 2$.

Now, define the first-layer sliding surfaces for actuated subsystem

$$\begin{cases}s_{11}=c_1e_1+e_2\\ s_{12}=c_2e_3+e_4\end{cases}\tag{12}$$

and for unactuated subsystem

$$\begin{cases}s_{13}=c_3e_{\theta_1}+\dot{e}_{\theta_1}\\ s_{14}=c_4e_{\theta_2}+\dot{e}_{\theta_2}\\ s_{15}=c_5e_r+\dot{e}_r\\ s_{16}=c_6e_\alpha+\dot{e}_\alpha\end{cases}\tag{13}$$

where $e_{\theta_1}=\theta_1-\theta_{1d}$, $e_{\theta_2}=\theta_2-\theta_{2d}$, $e_r=r-r_d$, $e_\alpha=\alpha-\alpha_d$ is the tracking error of the unactuated vector $\mathbf{q}_{ua}$ and c_i, $i=1, 2, \cdots, 6$ are positive constants.

The correlation between tether libration and deployment is established through the second-layer sliding surfaces, as the former is usually attributed to the Coriolis force that varies with tether deploy velocity.

Downloaded from https://spj.science.org at North China Electric Power University on July 31, 2024

$$\begin{cases} s_{21} = s_{11} - c_7 s_{13} \\ s_{22} = s_{12} - c_8 s_{14} \end{cases} \tag{14}$$

where c_7 and c_8 are positive constants.

Taking the derivative of Eq. 14 and let it equal to 0, one can obtain that

$$\begin{cases} u_{eq1} = \left(-g_1 f_{L1} - \ddot{L}_{1d} - k_1^2 \lambda_1 + \left(k_1 + k_2\right)\lambda_2 + c_1 e_2\right) \\ \qquad -c_7\left(-M_{33}^{-1} f_{\theta 1} - \ddot{\theta}_{1d} + c_3 \dot{e}_{\theta_1}\right) + \hat{d}_1 \\ u_{eq2} = \left(-g_2 f_{L2} - \ddot{L}_{2d} - k_3^2 \lambda_3 + \left(k_3 + k_4\right)\lambda_4 + c_2 e_4\right) \\ \qquad -c_8\left(-M_{44}^{-1} f_{\theta 2} - \ddot{\theta}_{2d} + c_4 \dot{e}_{\theta 3}\right) + \hat{d}_2 \end{cases} \tag{15}$$

where $\hat{d}_1$ is the estimation of acceleration term $d_1 = d_{L_1} - k_7 d_{\theta_1}$ and $\hat{d}_2$ is the estimation of $d_1 = d_{L_2} - k_8 d_{\theta_2}$ and will be given later.

Subsequently, the total HSMC law can be posited as

$$\begin{cases} u_1 = u_{eq1} + u_{sw} \\ u_2 = u_{eq2} + u_{sw} \end{cases} \tag{16}$$

where u_{sw} is the switching control law of the HSMC.

To include all information of the subsystems of TSS, the following manifold is defined as

$$\begin{cases} s_{23} = s_{15} + c_9 s_{16} \\ s_3 = s_{21} + h_{10} s_{22} + h_{11} s_{23} \end{cases} \tag{17}$$

Here, $h_{10} = c_{10}\, sgn\,(s_{21}s_{22})$, $h_{11} = c_{11}\, sgn\,(s_{21}s_{23})$, and c_9, c_{10}, c_{11} are positive constants.

Up to now, a 3-layer sliding surface for the whole TSS is constructed. Figure 3 depicts the hierarchical structure of sliding surfaces.

Figure 3 demonstrates that the third-layer sliding surface s_3 contains complete motion information of the TSS. Taking the derivative of s_3 and substituting Eq. 16 to Eq. 17 yields

Let

$$\dot{s}_3 = g_1 u_{sw} + h_{10} g_2 u_{sw} + h_{11} \dot{s}_{22} \tag{18}$$

$$\dot{s}_3 = -k s_3 - \eta \mathrm{sign}\left(s_3\right) \tag{19}$$

where k, η are positive constants. Then

$$u_{sw} = -\frac{k s_3 + \eta \mathrm{sign}\left(s_3\right) + h_{11}\hat{\dot{s}}_{22}}{g_1 + h_{10} g_2} \tag{20}$$

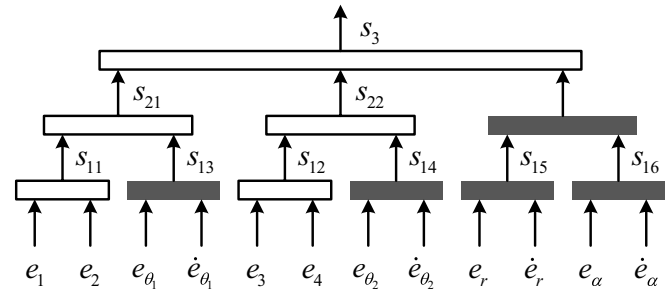

Fig. 3. Hierarchical structure of the sliding surfaces.

As obtaining the analytical expression of $\dot{s}_{22}$ poses a challenge, a sliding mode-based differentiator is introduced to estimate $\dot{s}_{22}$. The dynamics of the differentiator can be given as

$$\begin{cases} \dot{v}_0 = w_0 = -\lambda_2 L^{1/3}\left|v_0 - s_{22}\right|^{2/3}\mathrm{sign}\left(v_0 - s_{22}\right) + v_1 \\ \dot{v}_1 = w_1 = -\lambda_1 L^{1/3}\left|v_1 - w_0\right|^{2/3}\mathrm{sign}\left(v_1 - w_0\right) + v_2 \\ \dot{v}_2 = w_2 = -\lambda_0 L\mathrm{sign}\left(v_2 - w_1\right) \end{cases} \tag{21}$$

where L is a constant with a positive value. By selecting the parameters λ_0, λ_1, $\lambda_2 > 0$ properly, after a finite-time transient process, we have

$$v_0 = s_{22}, v_1 = \dot{s}_{22} \tag{22}$$

as a result, the estimation of $\dot{s}_{22}$ is $\hat{\dot{s}}_{22} = v_1$.

In Eq. 15, the acceleration signal is unmeasurable, and it is also difficult to reconstruct the acceleration through state derivative operation owing to measurement noise. Hence, a DO was introduced to estimate second derivative parts.

The design of the DO for the system (14) exploits the approach proposed in [28]

$$\begin{cases} \dot{z}_i = f_i(\mathbf{x}) + g_i(\mathbf{x})u_i + k_{1i}\mathrm{sig}^{p_i}\left(\sigma_i\right) + \hat{d}_i \\ \hat{d}_i = k_{2i}\mathrm{sig}^{q_i}\left(\sigma_i\right) \end{cases} \tag{23}$$

where $\hat{d}_i$ is the estimation of d_i, $\sigma_i = x_{2\cdot i} - z_i$ is an auxiliary variable, observer gains $k_{1i} > 0$ and $k_{2i} > 0$, and constants p_i and q_i satisfy $0.5 \leqslant p_i < 1$ and $q_i = 2p_i - 1$, respectively, $i = 1, 2$.

Theorem 1 *Considering TSAR system given by Eq.* 1 *and the control input obtained by Eq.* 16*, the tracking error will eventually converge to zero, which indicates the asymptotic stability of the closed-loop system.*

Numerical Simulation

This section uses MATLAB/Simulink to conduct computer simulations that validate the effectiveness of the proposed deployment scheme. The initial condition is shown in Table 1, and tether L_2 has been deployed to create a sequential deployment scene. The initial libration velocity in Table 1 was set to zero, which is advisable to stabilize the TSS before deployment to prevent tether winding in actual missions. What is

Downloaded from https://spj.science.org at North China Electric Power University on July 31, 2024

Table 1. TSS parameters.

Parameter name	Parameter value
Satellite mass m_1	2,000 kg
Satellite mass m_2, m_3	500 kg
Orbital geocentric distance r	6,627.145 km
True anomaly α	3.2531
Eccentricity e	2.71×10^{-3}
Final tether length L_{1f},L_{2f}	100 m
Switch tether length L_{s1}	90 m
Initial libration angle θ_{10} ,θ_{20}	0
Initial libration velocity $\dot{\theta}_{10}$, $\dot{\theta}_{20}$	0 rad/s

Table 2. Controller parameters.

Parameter description	Parameter name	Parameter value
Anti-windup module	k_1, k_2, k_3, k_4	0.05, 0.2, 0.2, 0.5
Sliding surfaces	$c_1, c_2, c_3, c_4, c_5, c_6$	0.05, 1, 2, 2, 0.004, 0.001
	c_7, c_8, c_9	1.2, 1.2, 1
	c_{10}, c_{11}	1, 1
	k, η, ε	1, 0.1, 0.01
Disturbance observer	k_{11}, k_{12}, p_1	1, 0.01, 0.98
	k_{21}, k_{22}, p_2	1, 0.01, 0.98
Robust differentiator	$\lambda_0, \lambda_1, \lambda_2, L$	1.1, 1.5, 2, 0.05

more, to avoid the singularity at $L_{10} = 0$m, the initial value $L_{10} = 2$m was used in the simulation, and the initial deployment rate $\dot{L}_{10} = 0.02\text{m}/\text{s}$.

The controller parameters are presented in Table 2. In HSMC, the sigmoid function $\text{sign}_{relay}(\sigma, \varepsilon)$ is utilized as an alternative to the signum function to generate a continuous and smooth control input in order to avoid control chattering.

To verify the effectiveness of the proposed deployment scheme (marked as Scheme 3), 2 alternative deployment schemes were used for comparison. In Scheme 1, the system is regarded as 2 independent 2-body, in which the tether length L_2 remains constant, and only tension T_1 is adjustable. In Scheme 2, the system is regarded as two 2-body, but the coupling between adjacent tethers is neglected. That is to say, tether L_1 only affects angle θ_1 and L_2 only affects θ_2. In Schemes 1 and 2, the deployment controller in [15] is adopted.

$$\begin{cases} u_1 = g_1^{-1}\left(\frac{1}{1+\alpha_1}\left(\alpha_1 p_1 \ddot{e}_{\theta_1} - c_1 e_2 - k_1\left((1+\alpha)e_2 - \alpha_1 p \dot{e}_{\theta_1} + c_1 e_1\right)\right) - \dot{e}_2\right) \\ u_2 = g_2^{-1}\left(\frac{1}{1+\alpha_2}\left(\alpha_2 p_2 \ddot{e}_{\theta_2} - c_2 e_4 - k_2\left((1+\alpha)e_4 - \alpha_2 p \dot{e}_{\theta_2} + c_2 e_3\right)\right) - \dot{e}_4\right) \end{cases} \tag{24}$$

where $\alpha_1 = \alpha_2 = 5, k_1 = k_2 = 2, p_1 = p_2 = 25, c_1 = 0.005, c_2 = 0.05$.

To prevent slackness or breakage of the tether, the tension in the above schemes is constrained by minimum value $T_{\min} = 0.01N$ and maximum value $T_{\max} = 1N$ (which is twice the tension reference command).

Figures 4 to 9 depict the simulation results. Figure 4 shows the length and velocity of tether L_1, while Fig. 5 shows the libration angle θ_1 and angular velocity $\dot{\theta}_1$. It can be observed that the tether deployment error and libration angle converge to zero asymptotically in 3 h (a little more than one orbital period) under Scheme 3. At the beginning of deployment, the angular velocity exhibits a negative trend caused by the Coriolis force, which is directly proportional to the tether deployment rate but with an opposite sign. Then, tether length increases, gravity torque increases, and following an amplitude decreases libration velocity. As a result, the libration velocity changes direction to positive and eventually decreases to zero. From Fig. 4, it can be seen that the deployment error under Schemes

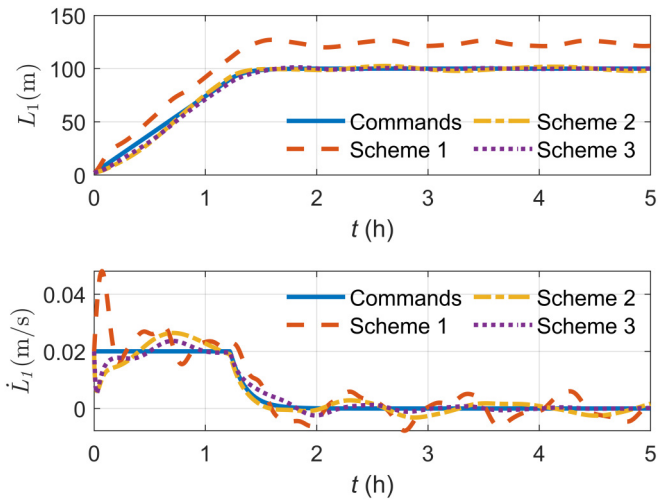

Fig. 4. Deployment length and velocity for tether L_1.

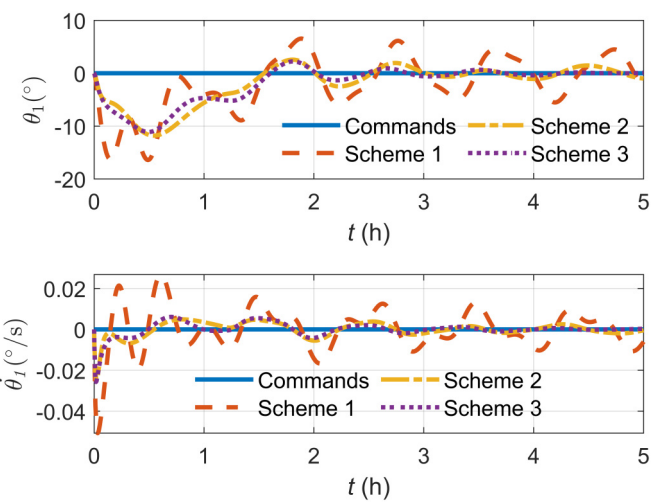

Fig. 5. Libration angle θ_1 and its angular velocity.

Downloaded from https://spj.science.org at North China Electric Power University on July 31, 2024

1 and 2 is quite larger than that under the proposed Scheme 3, which implies that the proposed scheme facilitates the rapid and efficient deployment of the tether L_1. From Fig. 5, the maximum in-plane angle is also a little smaller under the proposed scheme, and a larger in-plane angle will exacerbate the possibility of tether entanglement. In general, the deployment trajectories depicted in Figs. 4 and 5 indicate that Scheme 3 is a more favorable approach to the deployment process.

As mentioned in the "Deployment Strategies and Controllability Analysis" section, the control objective of L_2 is to eliminate (or reduce) the libration oscillation and to maintain the tether length error in a small range. Therefore, the proposed sliding surface coefficient in L_2 is larger than that in L_1 to punish changes in tether length. Figures 6 and 7 show the dynamic behavior of tether L_2. From Figs. 6 and 7, it is apparent that the proposed Scheme 3 offers a smaller tether deployment/retrieval length than Scheme 2. This means that significant control efforts could be saved under the proposed scheme.

The time responses of tension are depicted in Fig. 8. The results show that throughout the deployment process, the tether tension remains within the prescribed range, demonstrating the effectiveness of the proposed control scheme in addressing saturation effects. At about 1.25 h, deployment commands go from uniform to exponential, and there is only a slight influence on tether tension for the proposed control law. Finally, the tether tension is stabilized to the steady-state value, but there are still small fluctuations to reduce the libration oscillation by changing the tether length.

Finally, a comparison is made between Schemes 2 and 3 based on the integration of tracking error and tether tension, and the normalized results are illustrated in Fig. 9. Compared to Scheme 2, the proposed HSMC explicitly takes the 3-body TSS couple into account, resulting in faster and more accurate tether deployment with a smaller in-plane angle, which further shows that a fairly better deployment process is achieved under the proposed scheme.

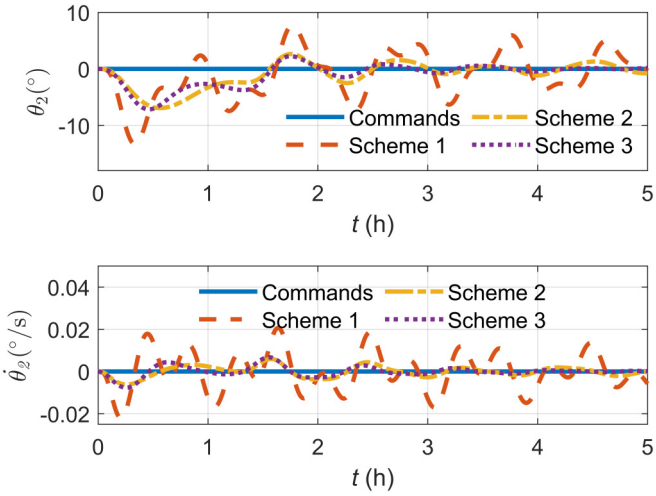

Fig. 6. Libration angle θ_2 and its angular velocity.

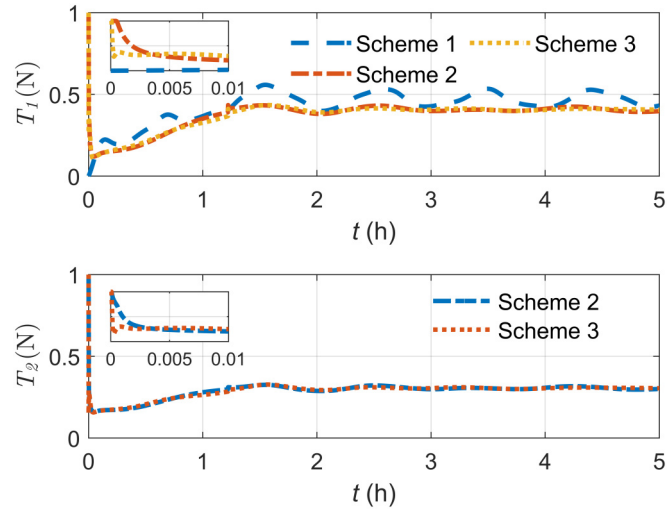

Fig. 8. Time history of tether tension.

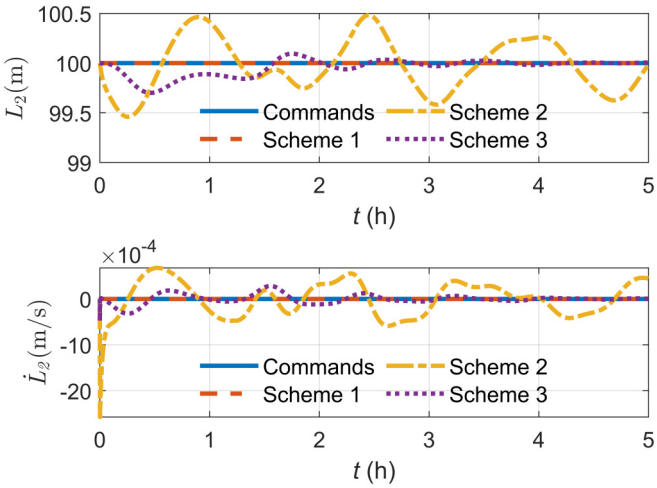

Fig. 7. Length and velocity for tether L_2.

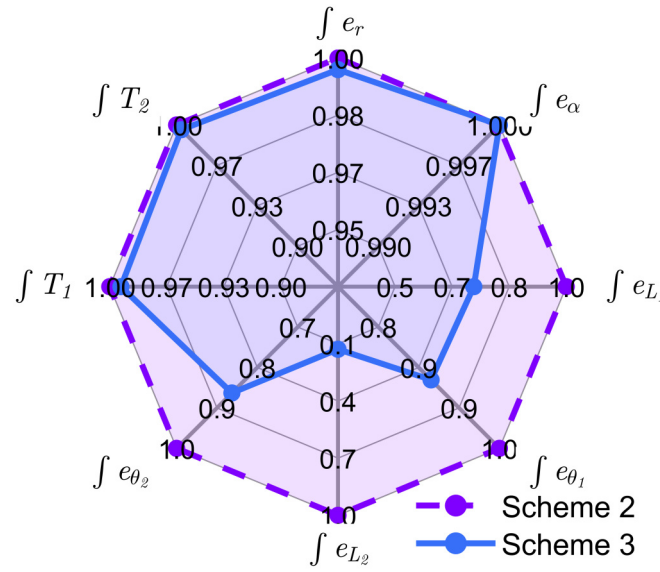

Fig. 9. Error and tension integral in Schemes 2 and 3.

Downloaded from https://spj.science.org at North China Electric Power University on July 31, 2024

Conclusions

The paper develops a new deployment strategy for the 3-body chain-type TSS. The distinctive feature of this paper is that the effect of the newly expanded satellite for TSS in a low-eccentric elliptical orbit is explicitly considered in the deployment scheme. First, the effects of the separation strategy are investigated. Then, an HSMC law embed with an auxiliary anti-windup system is developed. By dividing the underactuated model into 2 parts, actuated and unactuated subsystems, the acceleration signals for the actuated subsystem are produced by a finite-time DO, and the sliding surface and its time derivative for the unactuated subsystem are approximated by a robust differentiator. Finally, numerical simulations were carried out to confirm the effectiveness of the proposed deployment scheme. Future work may focus on how to achieve station-keeping for the chain-type tethered system.

Acknowledgments

Funding: This research is sponsored by the National Natural Science Foundation of China (grant number 62173273) and the Natural Science Basic Research Plan in Shaanxi Province of China (grant number 2020JC-19). **Author contributions:** C.J. contributed the central idea and analyzed most of the data. Z.M. and B.W. contributed to refining the ideas and carrying out additional analyses. All authors contributed to the writing and revisions. **Competing interests:** The authors declare that they have no competing interests.

Data Availability

Some or all data, models, or codes that support the findings of this study are available from the corresponding author upon reasonable request.

Supplementary Materials

Appendix

References

1. Rizzoli P, Martone M, Gonzalez C, Wecklich C, Borla Tridon D, Bräutigam B, Bachmann M, Schulze D, Fritz T, Huber M, et al. Generation and performance assessment of the global TanDEM-X digital elevation model. *ISPRS J Photogramm Remote Sens*. 2017;132:119–139.
2. Krieger G, Moreira A, Fiedler H, Hajnsek I, Werner M, Younis M, Zink M. TanDEM-X: A satellite formation for high-resolution SAR interferometry. *IEEE Trans Geosci Remote Sens*. 2007;45(11):3317–3341.
3. Moccia A, Vetrella S. A tethered interferometric synthetic aperture radar (SAR) for a topographic mission. *IEEE Trans Geosci Remote Sens*. 1992;30(1):103–109.
4. Carlson DF, Ozgokmen T, Novelli G, et al. Surface ocean dispersion observations from the ship-tethered aerostat remote sensing system. *Front Mar Sci*. 2018;5:00479.
5. Trushlyakov V, Yudintsev V. Dynamics of rotating tethered system for active debris removal. *Acta Astronaut*. 2022;195:405–415.
6. Zhao GW, Sun L, Huang H, Geng L. Optimal attitude control of a tethered system for noncoplanar orbital transfer under a constant thrust. *IEEE Trans Aerosp Electron Syst*. 2020;56(3):1844–1855.
7. Liu J, Liu B, Wu Z, Jiang J, Tian L. Dynamics and potential applications of a lunar space tethered system. *Acta Astronaut*. 2020;169:138–149.
8. Zakrzhevskii AE. Method of deployment of a space tethered system aligned to the local vertical. *J Astronaut Sci*. 2016;63:221–236.
9. Yu BS, Jin DP, Wen H. An analytical control law of length rate for tethered satellite system. *Meccanica*. 2017;52:2035–2046.
10. Wei C, Bian Y, Liao Y, Luo S, Yin Z, Luo J. ESO-based saturated deployment control of tethered satellite system with finite-time tracking performance guarantees. *IFAC-PapersOnLine*. 2020;53(2):5689–5694.
11. Liu C, Wang W, Guo Y, Chen S, Li A, Wang C. Neural network-based adaptive terminal sliding mode control for the deployment process of the dual-body tethered satellite system. *Proc Inst Mech Eng Part G J Aerospace Eng*. 2020;234(6):1157–1171.
12. Ma Z, Sun G, Cheng Z, Li Z. Pure-tension non-linear sliding mode control for deployment of tethered satellite system. *Proc Inst Mech Eng Part G: J Aerospace Eng*. 2018;232(13):2541–2551.
13. Xu S, Wen H, Huang Z, Jin D. A fuzzy control scheme for deployment of space tethered system with tension constraint. *Aerosp Sci Technol*. 2020;106:106143.
14. Xu SD, Sun GH, Ma ZQ, Li XL. Fractional-order fuzzy sliding mode control for the deployment of tethered satellite system under input saturation. *IEEE Trans Aerosp Electron Syst*. 2019;55(2):747–756.
15. Murugathasan L, Zhu ZH. Deployment control of tethered space systems with explicit velocity constraint and invariance principle. *Acta Astronaut*. 2019;157:390–396.
16. Yu BS, Huang Z, Geng LL, Jin DP. Stability and ground experiments of a spinning triangular tethered satellite formation on a low earth orbit. *Aerosp Sci Technol*. 2019;92:595–604.
17. Huang B, Zhang F, Song M, Huang P. Adaptive dynamic event-triggered deployment control for space triangle tethered formation system with external disturbance. *Acta Astronaut*. 2022;200:1–10.
18. Guang Z, Xingzi B, Bin L. Optimal deployment of spin-stabilized tethered formations with continuous thrusters. *Nonlin Dyn*. 2019;95:2143–2162.
19. Shi G, Zhu Z, Zhu ZH. Stable orbital transfer of partial space elevator by tether deployment and retrieval. *Acta Astronaut*. 2018;152:624–629.
20. Zhang JX, Cao XB, Wang JH, Lin XH. Configuration, orbit design of InSAR formation based on mean elements. *IEEE Trans Aerosp Electron Syst*. 2009;45(2):747–752.
21. Wang BH, Meng ZJ, Jia C, Huang PF. Reel-based tension control of tethered space robots. *IEEE Trans Aerosp Electron Syst*. 2020;56(4):3028–3043.
22. Williams P. Deployment/retrieval optimization for flexible tethered satellite systems. *Nonlin Dyn*. 2008;52(1):159–179.
23. Jung W, Mazzoleni AP, Chung J. Nonlinear dynamic analysis of a three-body tethered satellite system with deployment/retrieval. *Nonlin Dyn*. 2015;82(3):1–18.
24. Wang CQ, Wang PB, Li AJ, Guo Y. Deployment of tethered satellites in low-eccentricity orbits using adaptive sliding mode control. *J Aerosp Eng*. 2017;30(6):1.

Downloaded from https://spj.science.org at North China Electric Power University on July 31, 2024

25. Misra AK, Modi VJ. Deployment and retrieval of shuttle supported tethered satellites. *J Guid Control Dyn*. 1982;5(3): 278–285.
26. Wang DX, Jia YH, Jin L, Gui HC, Xu SJ. Controllability of an underactuated spacecraft with one thruster under disturbance. *Acta Mech Sinica*. 2012;28:838–847.
27. Meng Z, Wang B, Huang P. MPC-based anti-sway control of tethered space robots. *Acta Astronaut*. 2018;152:146–162.
28. Zhang J, Xu F, Liu X, Gu S, Geng H. Fixed-time dynamic surface control for pneumatic manipulator system with unknown disturbances. *IEEE Robot Autom Lett*. 2022;7(4):10890–10897.

Downloaded from https://spj.science.org at North China Electric Power University on July 31, 2024